International Journal of Heat and Mass Transfer 72 (2014) 98–113

Contents lists available at ScienceDirect

International Journal of Heat and Mass Transfer

journal homepage: www.elsevier.com/locate/ijhmt

# Turbulent heat transfer in a counterflow moving porous bed using a two-energy equation model

Marcelo J.S. de Lemos *, Ana C. Pivem

*Departamento de Energia – IEME, Instituto Tecnológico de Aeronáutica – ITA, 12228-900 São José dos Campos, SP, Brazil*

ARTICLE INFO

*Article history:*
Received 25 September 2013
Received in revised form 18 December 2013
Accepted 18 December 2013
Available online xxxx

*Keywords:*
Counterflow
Moving bed
Turbulence
Heat transfer
Porous media

ABSTRACT

This work investigates the influence of physical properties on heat transfer in a turbulent counterflow in a moving bed using the High and Low Reynolds number turbulence models, in which the working fluid flows in opposite direction to that of the steady movement of the permeable rigid medium. Transport equations for flow and heat transfer in a moving bed equipment are applied and discretized using the control-volume method. The system of algebraic equations obtained is relaxed via the SIMPLE algorithm. The effects of Reynolds number, solid-to-fluid velocity ratio, permeability, porosity, ratio of solid-to-fluid thermal capacity and ratio of solid-to-fluid thermal conductivity on heat transport are investigated. Results indicate that motion of solid material, contrary to the direction of the fluid, enhances heat transfer between phases. The same effect was observed for smaller Darcy number and porosity, as well as for higher solid-to-fluid thermal capacity and thermal conductivity ratios. When the intrinsic fluid velocity increases there is a greater conversion of mechanical kinetic energy into turbulence, increasing the final levels of the turbulent kinetic energy for both High and Low Reynolds number models.

© 2013 Elsevier Ltd. All rights reserved.

## 1. Introduction

Many applications in industry are concerned with turbulent flow through permeable beds. Among them one can mention moving bed technology in counterflow configuration. Examples about such technology are found in equipment for chemical compound separation, recuperation of petrochemical processes, drying of grains and seeds, removal of organic matter in affluents and in certain types of heat exchangers, just to mention a few applications. Within this context, Yang (2009) [1] showed numerical simulation of turbulent flow and heat transfer in heat exchangers fitted with porous media, where a permeable material was inserted in a heat exchanger to improve its process performance. There, the $k$–$\varepsilon$ model was applied to treat turbulence. Littman et al. (1995) [2], Mansoori et al. (2002) [3] and Zhang and Reese (2001) [4] presented studies about turbulent gas–solid transport, where [2] showed the effect of particle diameter, particle density and loading ratio on the effective drag coefficient in steady transport, [3] presented the thermo-mechanical modeling of turbulence heat transfer in gas–solid flows including particle collisions and [4] studied particle-gas turbulence interactions using a kinetic theory approach applied to granular flows. Turbulent flows in composite domains, involving both a finite porous medium and a clear region, have been also investigated in the literature [5,6].

Several studies on laminar and turbulent flow though permeable media in a number of configurations were conducted and compiled in a book [7]. In those studies, when analyzing heat transport through the phases composing the medium, both the local thermal equilibrium model (LTE) as well as thermal non-equilibrium approach (LTNE) where tackle [8]. For cases when the solid phase also moves, computations for a moving porous beds in parallel [9] and counterflow configurations, have been presented [10]. However, studies in [9,10] were restricted to the laminar flow regime.

The purpose of this contribution is to extend the work in [10], which was limited to laminar flow, to the turbulent regime. One should point out that when going from simulating a simpler laminar flow to accurately predicting turbulent flow regime within acceptable accuracy, not only a proper mathematical model has to be employed, but also the use of an adequate numerical scheme and stable solution algorithm have to be employed. And yet, it is the behavior of the turbulence kinetic energy associated with the flow that is an important result to be observed. Such quantity, evidently, cann ot be obtained with simpler laminar models.

The study herein includes investigation on heat transfer between phases when several flow and material parameters as varied, including the effect Reynolds number, slip ratio, permeability, as well as

* Corresponding author. Tel.: +55 12 3947 5860; fax: +55 12 3947 5842.
*E-mail address:* delemos@ita.br (M.J.S. de Lemos).

0017-9310/$ - see front matter © 2013 Elsevier Ltd. All rights reserved.
http://dx.doi.org/10.1016/j.ijheatmasstransfer.2013.12.051

## Nomenclature

| | |
|---|---|
| $A_i$ | interfacial area [m$^2$] |
| $a_i$ | interfacial area per unit volume, $a_i = A_i/\Delta V$ [m$^{-1}$] |
| $c_F$ | Forchheimer coefficient |
| $c_k$ | non-dimensional turbulence model constant |
| $c$'s | model constants |
| $D$ | particle diameter [m] |
| $\mathbf{D}$ | deformation rate tensor, $\mathbf{D} = [\nabla\mathbf{u} + (\nabla\mathbf{u})^T]/2$[s$^{-1}$] |
| $f_2$ | damping function |
| $f_\mu$ | damping function |
| $G^i$ | production rate of $\langle k\rangle^i$ due to the porous matrix |
| $H$ | distance between channel walls [m] |
| $k$ | turbulent kinetic energy per unit mass [m$^2$/s$^2$] |
| $\langle k\rangle^i$ | intrinsic (fluid) average of $k$ |
| $\langle k\rangle^v$ | volume (fluid + solid) average of $k$ |
| $K$ | permeability [m$^2$] |
| $L$ | channel length [m] |
| $p$ | thermodynamic pressure [N/m$^2$] |
| $\langle p\rangle^i$ | intrinsic (fluid) average of pressure $p$ [N/m$^2$] |
| $Re$ | Reynolds number based on $\bar{\mathbf{u}}_D$ |
| $Re_D$ | Reynolds number based on $\bar{\mathbf{u}}_{rel}$ |
| $\bar{\mathbf{u}}$ | microscopic time-averaged velocity vector [m/s] |
| $\langle\bar{\mathbf{u}}\rangle^i$ | intrinsic (fluid) average of $\bar{\mathbf{u}}$ [m/s] |
| $\bar{\mathbf{u}}_D$ | Darcy velocity vector, $\bar{\mathbf{u}}_D = \phi\langle\bar{\mathbf{u}}\rangle^i$ [m/s] |
| $\bar{\mathbf{u}}_{rel}$ | relative velocity based on total volume, $\bar{\mathbf{u}}_{rel} = \bar{\mathbf{u}}_D - \mathbf{u}_S$ [m/s] |
| $u_\tau$ | friction velocity [m/s] |
| $X$ | dimensionless coordinate |
| $y_+$ | dimensionless distance among wall and first node, $y^+ = \frac{y_w u_\tau}{\nu}$ |

*Greek*

| | |
|---|---|
| $\varepsilon$ | dissipation rate of $k$, $\varepsilon = \mu\overline{\nabla\mathbf{u}' : (\nabla\mathbf{u}')^T}/\rho$ [m$^2$/s$^3$] |
| $\langle\varepsilon\rangle^i$ | intrinsic (fluid) average of $\varepsilon$ |
| $\phi$ | porosity |
| $\mu$ | fluid dynamic viscosity [kg/(m s)] |
| $\mu_t$ | turbulent viscosity [kg/(m s)] |
| $\mu_{t_\phi}$ | macroscopic turbulent viscosity [kg/(m s)] |
| $\nu$ | kinematic viscosity [m$^2$/s] |
| $\rho$ | density [kg/m$^3$] |
| $\sigma_k, \sigma_\epsilon$ | non-dimensional constants |

*Subscript*

| | |
|---|---|
| $s$,$f$ | $s$ = solid, $f$ = fluid |

thermal capacity and thermal conductivity ratios between the moving solid phase and the permeating fluid. With that, a wider range of engineering systems can be analyses with the model detailed in [7].

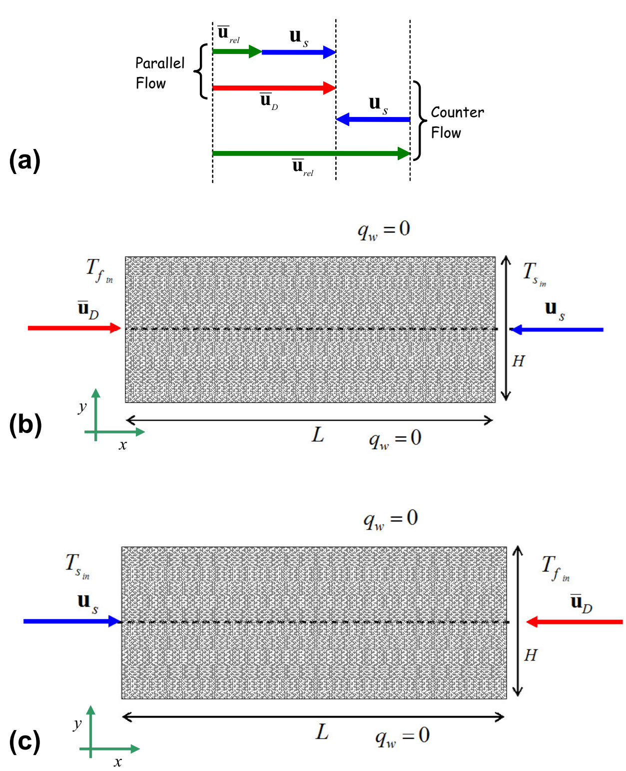


**Fig. 1.** Porous bed reactor with a moving solid matrix: (*a*) Flow configurations, (*b*) Counterflow with fluid moving west to east, (*c*) Counterflow with fluid moving east to west.

### 1.1. Macroscopic governing equations

The equations to follow are fully available in the open literature and for that their derivation are not repeated here [7]. Two possible

**Table 1**
Damping functions and constants for turbulence models.

| | High Reynolds number turbulence model proposed by Launder and Spalding (1974) [13] | Low Reynolds number turbulence model proposed by Abe et al. (1992) [14] |
|---|---|---|
| $f_\mu$ | 1.0 | $\left\{1-\exp\left[-\frac{(\nu\varepsilon)^{0.25}y}{14\nu}\right]\right\}^2\left\{1+\frac{5}{(k^2/\nu\varepsilon)^{0.75}}\exp\left[-\left(\frac{(k^2/\nu\varepsilon)}{200}\right)^2\right]\right\}$ |
| $f_2$ | 1.0 | $\left\{1-\exp\left[-\frac{(\nu\varepsilon)^{0.25}y}{3.1\nu}\right]\right\}^2\left\{1-0.3\exp\left[-\left(\frac{(k^2/\nu\varepsilon)}{6.5}\right)^2\right]\right\}$ |
| $\sigma_k$ | 1.0 | 1.4 |
| $\sigma_\varepsilon$ | 1.33 | 1.3 |
| $c_1$ | 1.44 | 1.5 |
| $c_2$ | 1.92 | 1.9 |

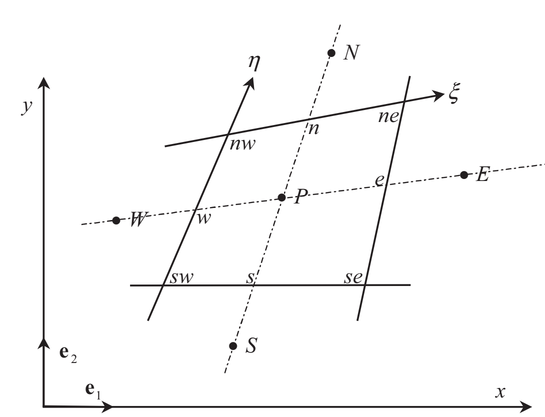


**Fig. 2.** Control volume and notation.

flow configurations can be analyzed as depicted in Fig. 1*a*. Both phases can co-flow in the same direction (*parallel flow*) or have opposite directions (*counterflow*). Here, only counterflow cases are investigated. Further, the geometry considered in this work is also schematically shown Fig. 1. The channel shown in the figure has length and height given by $L$ and $H$, respectively. For the sake of checking the computer code accuracy, two equivalent cases are here investigated. In the first case, the solid matrix moves from east to west whereas the fluid enters through the west side of the porous reactor, Fig. 1*b*. In an equivalent but reversed configuration, both solid and fluid exchange their side of entrance, Fig. 1*c*. Also, for a moving bed, only cases where the solid phase velocity is kept constant will be considered here, or say, we assume a moving bed with constant velocity that crosses a fixed control volume in addition to a counterflow fluid

A macroscopic form of the governing equations is obtained by taking the volumetric average of the entire equation set (Gray and Lee (1977) [11], Whitaker (1969) [12]. In this development, the porous medium is considered to be rigid, fixed, isotropic and saturated by the incompressible fluid. The final forms of the equations considered here are given by [7] and use a relative velocity defined as (Fig. 1*a*.),

$$\bar{\mathbf{u}}_{rel} = \bar{\mathbf{u}}_D - \mathbf{u}_S. \tag{1}$$

In addition, a relative Reynolds number based on $\bar{\mathbf{u}}_{rel}$ and $D$ can be defined as:

$$Re_D = \frac{\rho|\bar{\mathbf{u}}_{rel}|D}{\mu} \tag{2}$$

Further, if one uses the Darcy velocity and the overall reactor size $H$, one has a different definition for Reynolds given by,

$$Re = \frac{\rho|\bar{\mathbf{u}}_D|H}{\mu} \tag{3}$$

### 1.2. Flow equations

Incorporating all needed models, the final equations for turbulent flow read after volume averaging in addition to time averaging:

Continuity:

$$\nabla \cdot \bar{\mathbf{u}}_D = 0 \tag{4}$$

Momentum:

$$\begin{aligned} &\rho\left[\nabla \cdot \left(\frac{\bar{\mathbf{u}}_D\bar{\mathbf{u}}_D}{\phi}\right)\right] - \nabla \cdot \left\{\left(\mu + \mu_{t_\phi}\right)\left[\nabla\bar{\mathbf{u}}_D + (\nabla\bar{\mathbf{u}}_D)^T\right]\right\} \\ &\quad = -\nabla(\phi\langle\bar{p}\rangle^i) - \frac{\mu\phi}{K}\bar{\mathbf{u}}_{rel} + \frac{c_F\phi\rho|\bar{\mathbf{u}}_{rel}|\bar{\mathbf{u}}_{rel}}{\sqrt{K}}. \end{aligned} \tag{5}$$

where $\mu_{t_\phi}$ is the macroscopic eddy viscosity given by

$$\mu_{t_\phi} = \rho c_\mu f_\mu \frac{{\langle k\rangle^i}^2}{\langle\varepsilon\rangle^i}, \tag{6}$$

$c_\mu$ is a dimensionless constant and $f_\mu$ is a damping function, which differs from unit if a Low-Reynolds turbulence model is applied. Here, it is important to clarify the nomenclature used to classify turbulence models in regard to their ability to handle flows close to walls. For the so-called High Reynolds Turbulence Model (HRTM), a macroscopic form of the standard $k$–$\varepsilon$ closure was used (Launder and Spalding (1974) [13]). In such approach, the region close to the wall is bypassed and the velocity close to the surface is obtained via

**Table 2**
Cases and parameters used (High Reynolds Number Turbulence Model).

| Cases investigated | Dimensional | | | | Non-dimensional | | | | | | | |
|---|---|---|---|---|---|---|---|---|---|---|---|---|
| | $u_D$[m/s] | $u_S$[m/s] | $u_{rel}$[m/s] | $K$[m$^2$] | $Re_D$ | $Re$ | $u_S/u_D$ | $Da$ | $\phi$ | $(\rho c_p)_s/(\rho c_p)_f$ | $k_s/k_f$ | y+ |
| Effect of $Re_D$ | 1.416E01 | −7.083E00 | 2.125E01 | 1.000E-06 | 1.00E04 | 1.292E05 | −5.0E-01 | 1.665E-04 | 0.6 | 1.0E00 | 2.5E01 | 1.026E01 |
| | 7.083E01 | −3.542E01 | 1.062E02 | | 5.00E04 | 6.458E05 | | | | | | 4.901E01 |
| | 1.417E02 | −7.083E01 | 2.125E02 | | 1.00E05 | 1.292E06 | | | | | | 9.712E01 |
| | 1.417E03 | −7.083E02 | 2.125E03 | | 1.00E06 | 1.292E07 | | | | | | 9.528E02 |
| Effect of $u_S/u_D$ | 1.417E02 | 0.000E00 | 1.417E02 | 1.000E-06 | 6.67E04 | 1.292E06 | 0.0E00 | 1.665E-04 | 0.6 | 1.0E00 | 2.5E01 | 6.266E01 |
| | | −3.542E01 | 1.771E02 | | 8.33E04 | | −2.5E-01 | | | | | 7.960E01 |
| | | −7.083E01 | 2.125E02 | | 1.00E05 | | −5.0E-01 | | | | | 9.712E01 |
| | | −1.062E02 | 2.479E02 | | 1.17E05 | | −7.5E-01 | | | | | 1.150E02 |
| | | −1.346E02 | 2.762E02 | | 1.30E05 | | −9.5E-01 | | | | | 1.296E02 |
| Effect of $Da$ | 1.417E02 | −7.083E02 | 2.125E02 | 1.562E-08 | 1.25E04 | 1.292E06 | −5.0E-01 | 2.601E-06 | 0.6 | 1.0E00 | 2.5E01 | 1.138E02 |
| | | | | 1.406E-07 | 3.75E04 | | | 2.341E-05 | | | | 1.121E02 |
| | | | | 1.562E-06 | 1.25E05 | | | 2.601E-04 | | | | 9.267E01 |
| Effect of $\phi$ | 7.083E01 | −3.542E01 | 1.062E02 | 1.975E-07 | 5.00E04 | 6.458E05 | −5.0E-01 | 3.289E-05 | 0.4 | 1.0E00 | 2.5E01 | 6.175E01 |
| | | | | 1.000E-06 | | | | 1.665E-04 | 0.6 | | | 4.901E01 |
| | | | | 7.111E-06 | | | | 1.184E-03 | 0.8 | | | 3.122E01 |
| Effect of $(\rho c_p)_s/(\rho c_p)_f$ | 7.083E01 | −3.542E01 | 1.062E02 | 1.000E-06 | 5.00E04 | 6.458E05 | −5.0E-01 | 1.665E-04 | 0.6 | 2.5E-01 | 2.5E01 | 4.901E01 |
| | | | | | | | | | | 5.0E-01 | | |
| | | | | | | | | | | 1.0E00 | | |
| | | | | | | | | | | 1.0E01 | | |
| Effect of $k_s/k_f$, $u_S/u_{D=0}$ | 1.062E02 | 0.000E00 | 1.062E02 | 1.000E-06 | 5.00E04 | 9.688E05 | 0.0E00 | 1.665E-04 | 0.6 | 1.0E00 | 1.0E00 | 4.734E01 |
| | | | | | | | | | | | 1.0E01 | |
| | | | | | | | | | | | 1.0E02 | |
| | | | | | | | | | | | 1.0E03 | |
| Effect of $k_s/k_f$, $u_S/u_{D=0.1}$ | 9.659E01 | −9.659E00 | 1.062E02 | 1.000E-06 | 5.00E04 | 8.807E05 | −1.0E-01 | 1.665E-04 | 0.6 | 1.0E00 | 1.0E00 | 4.767E01 |
| | | | | | | | | | | | 1.0E01 | |
| | | | | | | | | | | | 1.0E02 | |
| | | | | | | | | | | | 1.0E03 | |
| Effect of $k_s/k_f$, $u_S/u_{D=0.4}$ | 7.589E01 | −3.036E02 | 1.062E02 | 1.000E-06 | 5.00E04 | 6.920E05 | −4.0E-01 | 1.665E-04 | 0.6 | 1.0E00 | 1.0E00 | 4.869E01 |
| | | | | | | | | | | | 1.0E01 | |
| | | | | | | | | | | | 1.0E02 | |
| | | | | | | | | | | | 1.0E03 | |

the wall log-law (see [13] for details). Essentially, when using a HRTM a given value for velocity close to the wall is used in lieu of the non-slip condition at the surface. Such value is calculated using the aforementioned wall log-law. On the other hand, when the region close to a surface is computed with a fine grid, resolving even the laminar sub-layer where grid points are laid, then the Low Reynolds Turbulence Model (LRTM) makes use of damping functions and constants which differ from the HRTM (additional information can be found in Abe et al. (1992) [14]). More details on damping functions and model constants for both wall models will be shown later.

Further, to obtain the eddy viscosity, $\mu_{t_\phi}$, we used here, as mentioned, the Low and High Reynolds number $k - \varepsilon$ models, whose equations for the turbulent kinetic energy and its dissipation rate, incorporating now a relative movement between the two phases $|\bar{\mathbf{u}}_{rel}|$, are given next.

A transport equation for $\langle k\rangle^i$ can be written as,

$$\rho[\nabla\cdot(\bar{\mathbf{u}}_D\langle k\rangle^i)] = \nabla\cdot\left[\left(\mu+\frac{\mu_{t_\phi}}{\sigma_k}\right)\nabla(\phi\langle k\rangle^i)\right] - \rho\langle\overline{\mathbf{u}'\mathbf{u}'}\rangle^i : \nabla\bar{\mathbf{u}}_D + \underbrace{c_k\rho\frac{\phi\langle k\rangle^i|\bar{\mathbf{u}}_{rel}|}{\sqrt{K}}}_{G^i} - \rho\phi\langle\varepsilon\rangle^i \tag{7}$$

where $\sigma_k$ and $c_k$ are dimensionless constants and the generation rate due to the porous substrate, $G^i$, which is included in Eq. (7), depends on $|\bar{\mathbf{u}}_{rel}|$ and reads,

$$G^i = c_k\rho\phi\langle k\rangle^i|\bar{\mathbf{u}}_{rel}|/\sqrt{K} \tag{8}$$

A corresponding transport equation for $\langle\varepsilon\rangle^i$, incorporating also the relative velocity $|\bar{\mathbf{u}}_{rel}|$, can be written as,

$$\rho\left[\frac{\partial}{\partial t}(\phi\langle\varepsilon\rangle^i) + \nabla\cdot(\bar{\mathbf{u}}_D\langle\varepsilon\rangle^i)\right] = \nabla\cdot\left[(\mu+\frac{\mu_{t_\phi}}{\sigma_\varepsilon})\nabla(\phi\langle\varepsilon\rangle^i)\right] + c_1(-\rho\langle\overline{\mathbf{u}'\mathbf{u}'}\rangle^i : \nabla\bar{\mathbf{u}}_D)\frac{\langle\varepsilon\rangle^i}{\langle k\rangle^i} + c_2c_k\rho\frac{\phi\langle\varepsilon\rangle^i|\bar{\mathbf{u}}_{rel}|}{\sqrt{K}} - c_2f_2\rho\phi\frac{\langle\varepsilon\rangle^{i2}}{\langle k\rangle^i} \tag{9}$$

where $\sigma_\varepsilon$, $c_1$ and $c_2$ are constants and $f_2$ is a damping function, $\bar{\mathbf{u}}_D$ is Darcy velocity vector, $\bar{\mathbf{u}}_D = \phi\langle\bar{\mathbf{u}}\rangle^i$, $\phi$ is the porosity, $\rho$ is the density of the fluid, $p$ is the pressure, $\mu$ is the fluid dynamic viscosity, $K$ is the medium permeability, $c_F$ is the Forchheimer coefficient, $\mu_{t_\phi}$ is the macroscopic turbulent viscosity, $\sigma_k$ and $\sigma_\varepsilon$ are constants, $\langle k\rangle^i$ is the intrinsic (fluid) average of $k$ and $\langle\epsilon\rangle^i$ is the intrinsic dissipation rate of $\langle k\rangle^i$, $\varepsilon = \mu\overline{\nabla\mathbf{u}' : (\nabla\mathbf{u}')^T}/\rho$. In Eq. (9), $c_1$ and $c_2$ are constants, $P^i = -\rho\langle\overline{\mathbf{u}'\mathbf{u}'}\rangle^i : \nabla\bar{\mathbf{u}}_D$ is the production rate of $\langle k\rangle^i$ due to gradients of $\bar{\mathbf{u}}_D$ and $G^i = c_k\rho\phi\langle k\rangle^i|\bar{\mathbf{u}}_D|/\sqrt{K}$ is the generation rate of the intrinsic average of $k$ due to the action of the porous matrix (see [7] for details).

### 1.3. Two-energy equation model

As for the flow, the macroscopic equations to heat transport in porous media are obtained by applying the average volume to microscopic equations. The mathematical model used to describe the heat transfer between the solid and fluid in a unit of moving bed is based on the two-energy equations model, which can be written as:

**Table 3**
Cases and parameters used (Low Reynolds Number Turbulence Model).

| Cases investigated | Dimensional | | | | Non-dimensional | | | | | | | |
|---|---|---|---|---|---|---|---|---|---|---|---|---|
| | $u_D$[m/s] | $u_S$[m/s] | $u_{rel}$[m/s] | $K$[m$^2$] | $Re_D$ | $Re$ | $u_S/u_D$ | $Da$ | $\phi$ | $(\rho c_p)_s/(\rho c_p)_f$ | $k_s/k_f$ | y+ |
| Effect of $Re_D$ | 1.771E00<br>3.542E00<br>7.083E00 | −8.854E−01<br>−1.770E00<br>−3.542E00 | 2.656E00<br>5.312E00<br>1.062E01 | 1.000E−06 | 1.25E03<br>2.50E03<br>5.00E03 | 1.615E04<br>3.229E04<br>6.458E04 | −5.0E−01 | 1.665E−04 | 0.6 | 1.0E00 | 2.5E01 | 8.67E−01<br>1.47E00<br>2.53E00 |
| Effect of $u_S/u_D$ | 1.062E01 | 0.000E00<br>−2.656E00<br>−5.312E00<br>−7.968E00<br>−1.009E02 | 1.062E01<br>1.325E01<br>1.594E01<br>1.859E01<br>2.072E01 | 1.000E−06 | 5.00E03<br>6.23E03<br>7.50E03<br>8.75E03<br>9.75E03 | 9.687E04 | 0.0E00<br>−2.5E−01<br>−5.0E−01<br>−7.5E−01<br>−9.5E−01 | 1.665E−04 | 0.6 | 1.0E00 | 2.5E01 | 3.15E00<br>3.29E00<br>3.41E00<br>3.51E00<br>3.59E00 |
| Effect of $Da$ | 1.417E01 | −7.083E00 | 2.125E01 | 1.562E−08<br>1.406E−07<br>1.562E−06 | 1.25E03<br>3.75E03<br>1.25E04 | 1.292E05 | −5.0E−01 | 2.601E−06<br>2.341E−05<br>2.601E−04 | 0.6 | 1.0E00 | 2.5E01 | 4.46E00<br>4.33E00<br>4.09E00 |
| Effect of $\phi$ | 3.542E00 | −1.771E00 | 5.312E00 | 1.975E−07<br>1.000E−06<br>7.111E−06 | 2.50E03 | 3.229E04 | −5.0E−01 | 3.289E−05<br>1.665E−04<br>1.184E−03 | 0.4<br>0.6<br>0.8 | 1.0E00 | 2.5E01 | 1.70E00<br>1.47E00<br>1.24E00 |
| Effect of $(\rho c_p)_s/(\rho c_p)_f$ | 3.542E00 | −1.771E00 | 5.312E00 | 1.000E−06 | 2.50E03 | 3.229E04 | −5.0E−01 | 1.665E−04 | 0.6 | 2.5E−01<br>5.0E−01<br>1.0E00<br>1.0E01 | 2.5E01 | 1.47E00 |
| Effect of $k_s/k_f$, $u_S/u_D = 0$ | 5.312E00 | 0.000E00 | 5.312E00 | 1.000E−06 | 2.50E03 | 4.844E04 | 0.0E00 | 1.665E−04 | 0.6 | 1.0E00 | 1.0E00<br>1.0E01<br>1.0E02<br>1.0E03 | 1.86E00 |
| Effect of $k_s/k_f$, $u_S/u_D = 0.1$ | 4.829E00 | −4.829−01 | 5.312E00 | 1.000E−06 | 2.50E03 | 4.403E04 | 1.0E−01 | 1.665E−04 | 0.6 | 1.0E00 | 1.0E00<br>1.0E01<br>1.0E02<br>1.0E03 | 1.76E00 |
| Effect of $k_s/k_f$, $u_S/u_D = 0.4$ | 3.795E00 | −1.518E00 | 5.312E00 | 1.000E−06 | 2.50E03 | 3.460E04 | 4.0E−01 | 1.665E−04 | 0.6 | 1.0E00 | 1.0E00<br>1.0E01<br>1.0E02<br>1.0E03 | 1.52E00 |

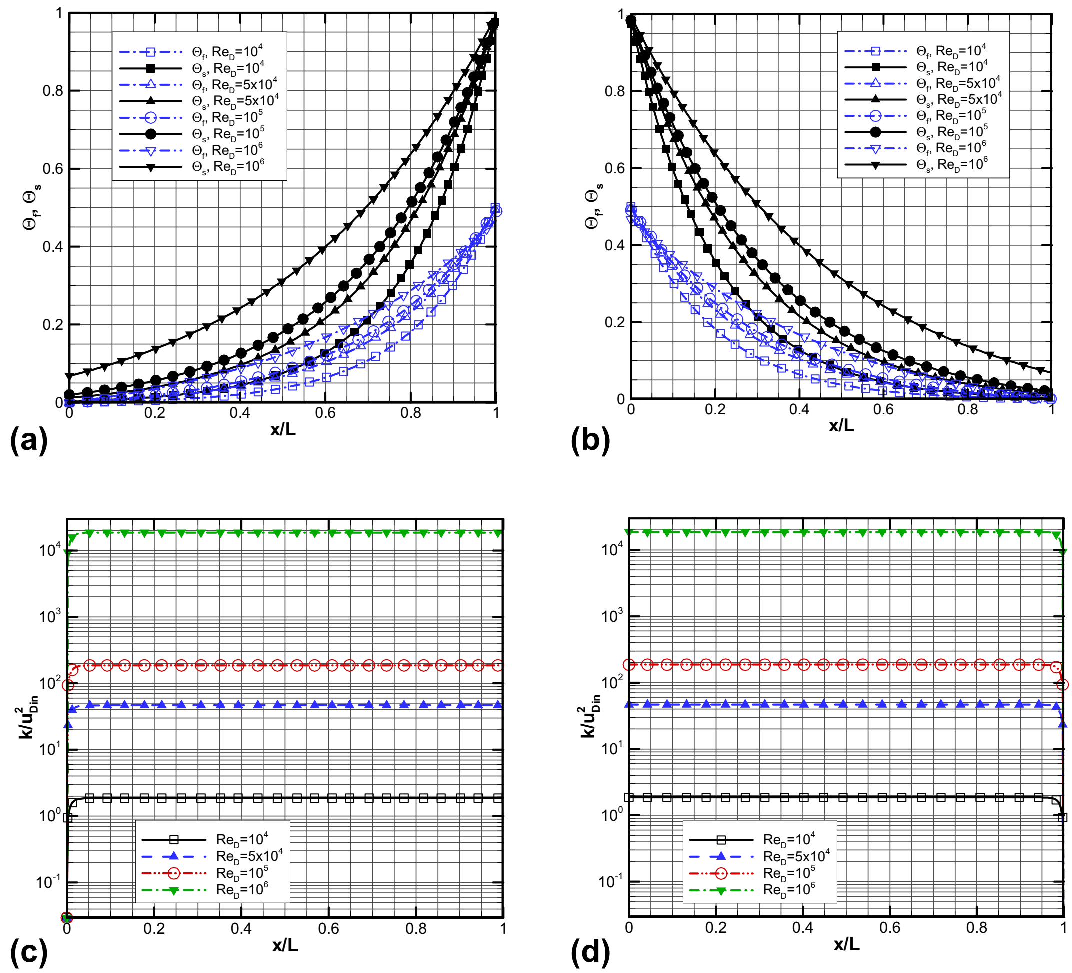


**Fig. 3.** Non-dimensional temperatures and turbulent kinetic energy for High Reynolds number turbulence model as a function of $Re_D$, with $u_S/\bar{u}_D = -0.5$; $k_s/k_f = 25$; $Da = 1.665 \times 10^{-4}$, $(\rho c_p)_s/(\rho c_p)_f = 1$, $\phi = 0.6$: (*a*), (*c*) Flow moving west to east, (*b*), (*d*). Flow moving east to west.

$$(\rho c_p)_f \nabla \cdot \left(\bar{\mathbf{u}}_D \langle \overline{T_f} \rangle^i\right) = \nabla \cdot \left\{\mathbf{K}_{eff,f} \cdot \nabla \langle \overline{T_f} \rangle^i\right\} + h_i a_i \left(\langle \overline{T_s} \rangle^i - \langle \overline{T_f} \rangle^i\right) \quad (10)$$

$$(\rho c_p)_s \nabla \cdot \left(\mathbf{u}_S \langle \overline{T_s} \rangle^i\right) = \nabla \cdot \left\{\mathbf{K}_{eff,s} \cdot \nabla \langle \overline{T_s} \rangle^i\right\} - h_i a_i \left(\langle \overline{T_s} \rangle^i - \langle \overline{T_f} \rangle^i\right) \quad (11)$$

where, $\mathbf{K}_{eff,f}$ and $\mathbf{K}_{eff,s}$ are the effective conductivity tensors for fluid and solid, respectively, given by:

$$\mathbf{K}_{eff,f} = [\phi k_f]\ \mathbf{I} + \mathbf{K}_{f,s} + \mathbf{K}_{disp} + \mathbf{K}_{disp,t} + \mathbf{K}_t \quad (12)$$

$$\mathbf{K}_{eff,s} = [(1-\phi)k_s]\ \mathbf{I} + \mathbf{K}_{s,f} \quad (13)$$

The terms $\mathbf{K}_{f,s}$, $\mathbf{K}_{f,s}$, $\mathbf{K}_t$, $\mathbf{K}_{disp}$, and $\mathbf{K}_{disp,t}$ are respectively, the local conduction tensors between fluid and solid, turbulent heat flow, thermal dispersion and turbulent thermal dispersion. $\mathbf{I}$ is the unit tensor and $\mathbf{K}_{disp}$, $\mathbf{K}_{f,s}$ and $\mathbf{K}_{s,f}$ are coefficients defined as,

Local conduction:

$$\begin{cases} \frac{1}{\Delta V} \int_{A_i} \mathbf{n}_i k_f \overline{T_f} dA = \mathbf{K}_{f,s} \cdot \nabla \langle \overline{T_s} \rangle^i \\ \frac{1}{\Delta V} \int_{A_i} \mathbf{n}_i k_s \overline{T_s} dA = \mathbf{K}_{s,f} \cdot \nabla \langle \overline{T_f} \rangle^i \end{cases}$$

where $\mathbf{n}_i$ in Eq. (14) is the unit vector pointing outwards of the fluid phase and $A_i$ is the interfacial area between the two phases.

Turbulent heat flow:'

$$-(\rho c_p)_f \left(\phi\ \overline{\langle \mathbf{u}' \rangle^i \langle T_f' \rangle^i}\right) = \mathbf{K}_t \cdot \nabla \langle \overline{T_f} \rangle^i \quad (15)$$

Thermal dispersion:

$$-(\rho c_p)_f \left(\phi\ \langle {}^i\bar{\mathbf{u}}\, {}^i\overline{T_f} \rangle^i\right) = \mathbf{K}_{disp} \cdot \nabla \langle \overline{T_f} \rangle^i \quad (16)$$

Turbulent thermal dispersion:

$$-(\rho c_p)_f \left(\phi\ \langle \overline{{}^i\mathbf{u}' {}^iT_f'} \rangle^i\right) = \mathbf{K}_{disp,t} \cdot \nabla \langle \overline{T_f} \rangle^i \quad (17)$$

In this work, for simplicity, one assumes that the overall thermal resistance between the two phases is controlled by the interfacial film coefficient, rather than by the thermal resistance within each phase. As such, the local conduction coefficients $\mathbf{K}_{f,s}$, $\mathbf{K}_{s,f}$ are here neglected for the sake of simplicity. Additional information on the models in Eqs. (12), and (13) can be found in [15].

### 1.4. Interfacial heat transfer coefficient

In Eqs. (10), and (11) the heat transferred between the two phases was modeled by means of a film coefficient, $h_i$, such that:

$$h_i a_i \left(\langle \overline{T_s} \rangle^i - \langle \overline{T_f} \rangle^i\right) = \frac{1}{\Delta V} \int_{A_i} \mathbf{n}_i \cdot k_f \nabla \overline{T_f}\, dA = \frac{1}{\Delta V} \int_{A_i} \mathbf{n}_i \cdot k_s \nabla \overline{T_s}\, dA. \quad (18)$$

where $a_i = A_i/\Delta V$ .

For numerically determining $h_i$, Kuwahara et al. (2001) [16] modeled a porous medium by considering it as an infinite number of solid square rods of size $D$, arranged in a regular triangular pattern. They numerically solved the governing equations in the

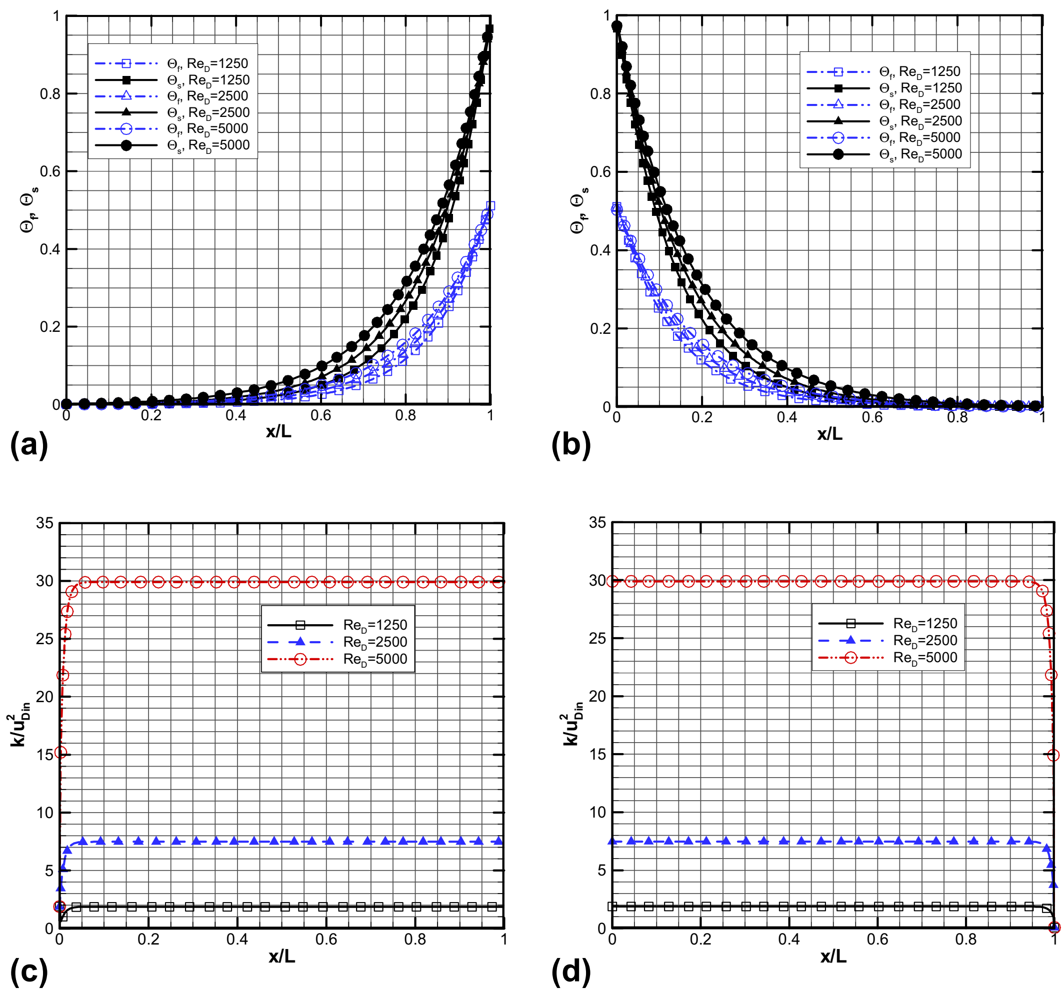


**Fig. 4.** Non-dimensional temperatures and turbulent kinetic energy for Low Reynolds number turbulence model as a function of $Re_D$, with $u_S/\bar{u}_D = -0.5$; $k_s/k_f = 25$; $Da = 1.665 \times 10^{-4}$, $(\rho c_p)_s/(\rho c_p)_f = 1$, $\phi = 0.6$: (*a*), (*c*) Flow moving west to east, (*b*), (*d*). Flow moving east to west.

void region, exploiting to advantage the fact that for an infinite and geometrically ordered medium a repetitive cell can be identified. Periodic boundary conditions were then applied for obtaining the temperature distribution under fully developed flow conditions.

For turbulent flow, Saito and de Lemos (2006) [15] extended the work in [17] for $Re_D$ up to $10^7$. Both Low Reynolds and High Reynolds turbulence models were applied in [15]. The following expression was proposed in [15]:

$$\frac{h_i D}{k_f} = 0.08\left(\frac{Re_D}{\phi}\right)^{0.8} Pr^{1/3};\ \text{for } 1.0\text{x}10^4 < \frac{Re_D}{\phi} < 2.0\text{x}10^7,\ \text{valid for } 0.2 < \phi < 0.9, \tag{19}$$

The interstitial heat transfer coefficient $h_i$ is calculated by correlations Eq. (19) for turbulent flow. However, since the relative movement between phases is seen as the promoter of convective heat transport from the fluid to the solid, or vice versa, the Reynolds number is used in the correlation Eq. (19) instead of a Reynolds number based on the absolute velocity of the fluid phase. Accordingly, when the solid phase velocity approaches the fluid velocity, the only mechanism for transferring heat between phases is conduction.

### 1.5. Wall treatment and boundary conditions

In this work, two forms of the $k$–$\varepsilon$ model are employed, namely the High Reynolds and Low Reynolds number turbulence models. For the High Reynolds turbulence model, a macroscopic form of the standard $k$–$\varepsilon$ closure was used (Launder and Spalding (1974) [13]) whereas for the Low Reynolds number model constants and damping functions of Abe et al. (1992) [14] were applied. All model constants and damping functions for both turbulence models are compiled in Table 1.

Boundary conditions are given by:

On the solid walls (Low Reynolds turbulence model):

$$\bar{u} = 0, \quad \langle \bar{\mathbf{u}} \rangle^i = 0, \quad k = 0, \quad \varepsilon = \nu \frac{\partial^2 k}{\partial y^2} \tag{20}$$

On the solid walls (High Reynolds turbulence model):

$$\frac{\bar{u}}{u_\tau} = \frac{1}{\kappa} \ln(y^+ E), \quad k = \frac{u_\tau^2}{c_\mu^{1/2}}, \quad \varepsilon = \frac{c_\mu^{3/4} k_w^{3/2}}{\kappa y_w} \tag{21}$$

with, $u_\tau = \left(\frac{\tau_w}{\rho}\right)^{1/2}$, $y_w^+ = \frac{y_w u_\tau}{\nu}$, where, $u_\tau$ is wall-friction velocity, $y_w$ is the non-dimensional coordinate normal to wall, $\kappa$ is the von Kármán constant, and $E$ is a constant that depends on the roughness of the wall.

For the west and east faces, boundary conditions will depend on the direction of fluid and feed stream as depicted in Fig. 1, as follows:

Case of Fig. 1*b* – counterflow with fluid moving west to east:

On the west face:

$$\bar{\mathbf{u}}_D = \mathbf{u}_{inlet}, \quad \langle \overline{T}_f \rangle^i = T_{f_{in}} \tag{22}$$

$$\langle \overline{T}_s \rangle^i = T_{s_{out}} \approx T_{f_{in}} + \frac{\frac{\partial}{\partial x}\left( (\rho c_p)_f u_{inlet} \langle \overline{T}_f \rangle^i - \phi k_f \frac{\partial \langle \overline{T}_f \rangle^i}{\partial x} \right)\Big|_{x=0}}{h_i a_i} \tag{23}$$

On east face:

$$\mathbf{u}_s = \mathbf{u}_{s_{in}}, \langle \overline{T}_s \rangle^i = T_{s_{in}} \tag{24}$$

$$\langle \overline{T}_f \rangle^i = T_{f_{out}} \approx T_{s_{in}} + \frac{\frac{\partial}{\partial x}\left( (\rho c_p)_s u_{s_{in}} \langle \overline{T}_s \rangle^i - (1-\phi) k_s \frac{\partial \langle \overline{T}_s \rangle^i}{\partial x} \right)\Big|_{x=L}}{h_i a_i} \tag{25}$$

Boundary conditions (23) and (25) come from applying the corresponding transport equations (10) and (11), in their steady-state form, at west and east faces, respectively.

Case of Fig. 1*c* - counterflow with fluid moving east to west:

On the west face:

$$\mathbf{u}_s = \mathbf{u}_{s_{in}}, \quad \langle \overline{T}_s \rangle^i = T_{s_{in}} \tag{26}$$

$$\langle \overline{T}_f \rangle^i = T_{f_{out}} \approx T_{s_{in}} + \frac{\frac{\partial}{\partial x}\left( (\rho c_p)_s u_{s_{in}} \langle \overline{T}_s \rangle^i - (1-\phi) k_s \frac{\partial \langle \overline{T}_s \rangle^i}{\partial x} \right)\Big|_{x=0}}{h_i a_i} \tag{27}$$

On east face:

$$\bar{\mathbf{u}}_D = \mathbf{u}_{inlet}, \quad \langle \overline{T}_f \rangle^i = T_{f_{in}} \tag{28}$$

$$\langle \overline{T}_s \rangle^i = T_{s_{out}} \approx T_{f_{in}} + \frac{\frac{\partial}{\partial x}\left( (\rho c_p)_f u_{inlet} \langle \overline{T}_f \rangle^i - \phi k_f \frac{\partial \langle \overline{T}_f \rangle^i}{\partial x} \right)\Big|_{x=L}}{h_i a_i} \tag{29}$$

Before leaving this section, it is interesting to say a word about the practical application of the inlet boundary conditions above. Real world engineering flows, in actual reactors, will most likely present a temperature distribution when the incoming flow, of either phase, is not well-insulated. However, when the feed stream is thermally isolated and the working fluid is well mixed and evenly distributed before entering the reactor, the use of constant temperature values at inlet may well represent the basic features of flow and heat transfer in such equipment. Example of similar boundary conditions assuming constant values at inlet for moving beds are found in reference [19].

### 1.6. Numerical method

The numerical method used to discretize the flow equations was based on the control volume approach. A schematic of node labeling for a general non-orthogonal two-dimensional grid is presented in Fig. 2. The SIMPLE method of Patankar (1980) [18] was used to the handle the pressure–velocity coupling and applied to relax the systems of algebraic equations.

The discretized form of the two-dimensional conservation equation for a generic property $\boldsymbol{\varphi}$ (tensor of any order) in steady-state reads,

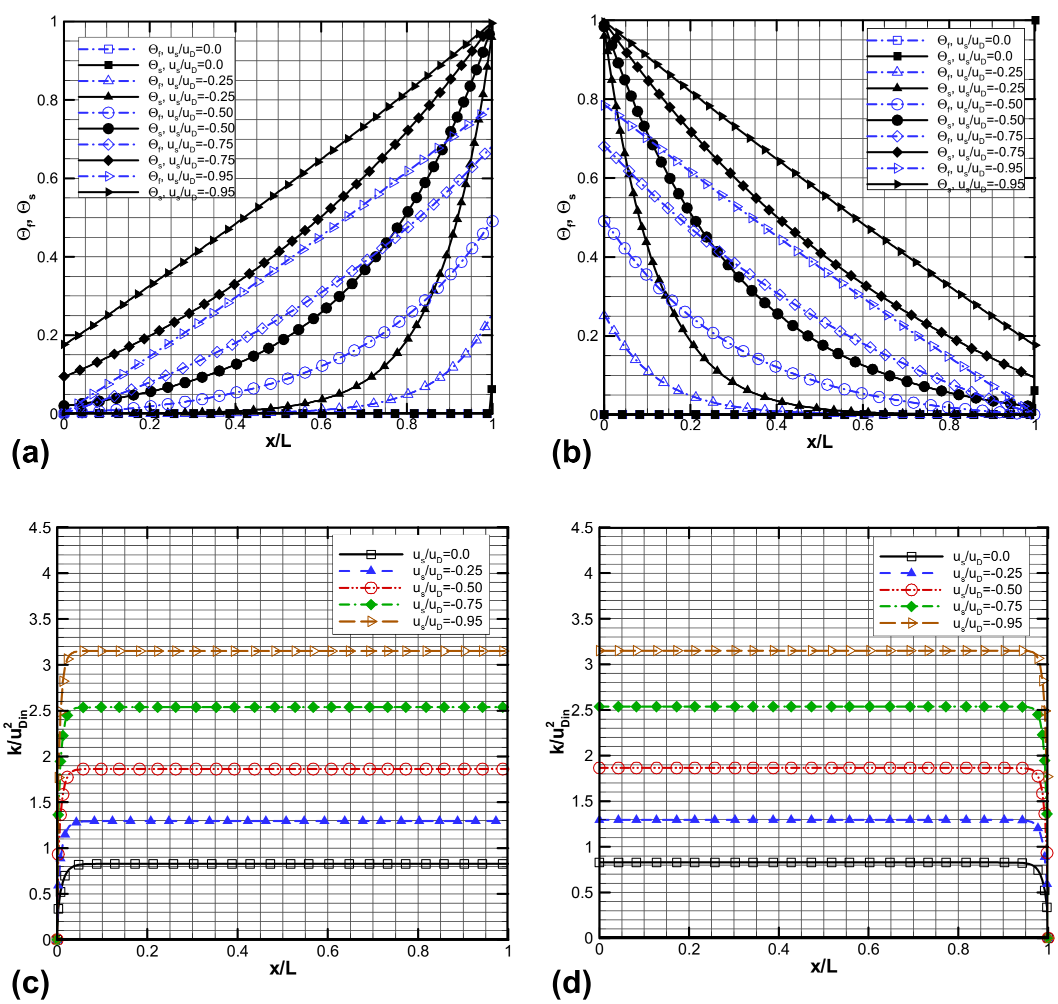


**Fig. 5.** Non-dimensional temperatures and turbulent kinetic energy for High Reynolds number turbulence model as a function of $u_S/u_D$, with $k_s/k_f = 25$, $\phi = 0.6$, $Da = 1.665 \times 10^{-4}$, $(\rho c_p)_s/(\rho c_p)_f = 1$, $Re = 1.292 \times 10^6$: (*a*), (*c*) Flow moving west to east, (*b*), (*d*). Flow moving east to west.

$$I_e + I_w + I_n + I_s = S_\varphi \tag{30}$$

where $I_e$, $I_w$, $I_n$ and $I_s$ represent, respectively, the fluxes of $\boldsymbol{\varphi}$ in the east, west, north and south faces of the control volume. $S_\varphi$ represents the source term, whose standard linearization is accomplished by making,

$$S_\varphi \approx S_\varphi^{**}\ \phi_P\ \langle\varphi\rangle_p^i + S_\varphi^{*} \tag{31}$$

where $\phi_P$ is the porosity of node $P$ (see Fig. 2). Discretization of the momentum equation in the $x$-direction gives further,

$$S^{*x} = (S_e^{*x})_P - (S_w^{*x})_P + (S_n^{*x})_P - (S_s^{*x})_P + S_P^{*} \tag{32}$$

$$S^{**x} = S_\phi^{**} \tag{33}$$

where, $S^{*x}$ is composed by part of the diffusion fluxes that are treated explicitly and by the pressure gradient term. The term, $S^{**x}$, entails the additional drag forces due to the porous matrix. Further, for the sake of simplicity, when discretizing Eq. 5 the relative velocity was considered only in the last term on the right-hand-side of it. Since this term is responsible for most of the drag on the fluid, such simplification did not impact on the trends of the results to be shown later.

Convergence was monitored in terms of the normalized residue, which was set to be lower than $10^{-9}$.

The two cases considered here are depicted in Fig. 1*b*,*c* and the only difference between them is the reversal, in the $x$-direction, of the boundary conditions applied for both velocities at their entrances. The sole reason for considering such two possibilities was to guarantee computer accuracy when comparing the solutions obtained with the two cases, which should present a perfect "mirror image" with respect to each other. Here, as in [10], showing symmetrical but identical results, by inverting the movement of both phases, was a way to double-check the code for any possible flaw when the many parameters were varied, including the Reynolds number, the slip ratio, the Darcy number as well as the thermal capacity and thermal conductivity ratios.

## 2. Results and discussion

As mentioned, Fig. 1*a* shows two possibilities for the relative movement of phases. Here, only counterflow cases are investigated.

The porous matrix moves with constant velocity $\mathbf{u}_s$ in opposite direction to the fluid velocity $\bar{\mathbf{u}}_D$ (see Fig. 1*a*). In the following figures, axial temperature profiles for both phases are presented for the two cases in Fig. 1*b* and *c* with the sole purpose to show that results will be consistent with application of reserved boundary conditions.

The fluid and solid phases are given different temperatures at the inlet and non-dimensional temperatures for the solid and fluid are defined as:

$$\theta_{s,f} = \frac{\langle \overline{T}_{s,f}\rangle^i - T_{\min}}{T_{\max} - T_{\min}} \tag{34}$$

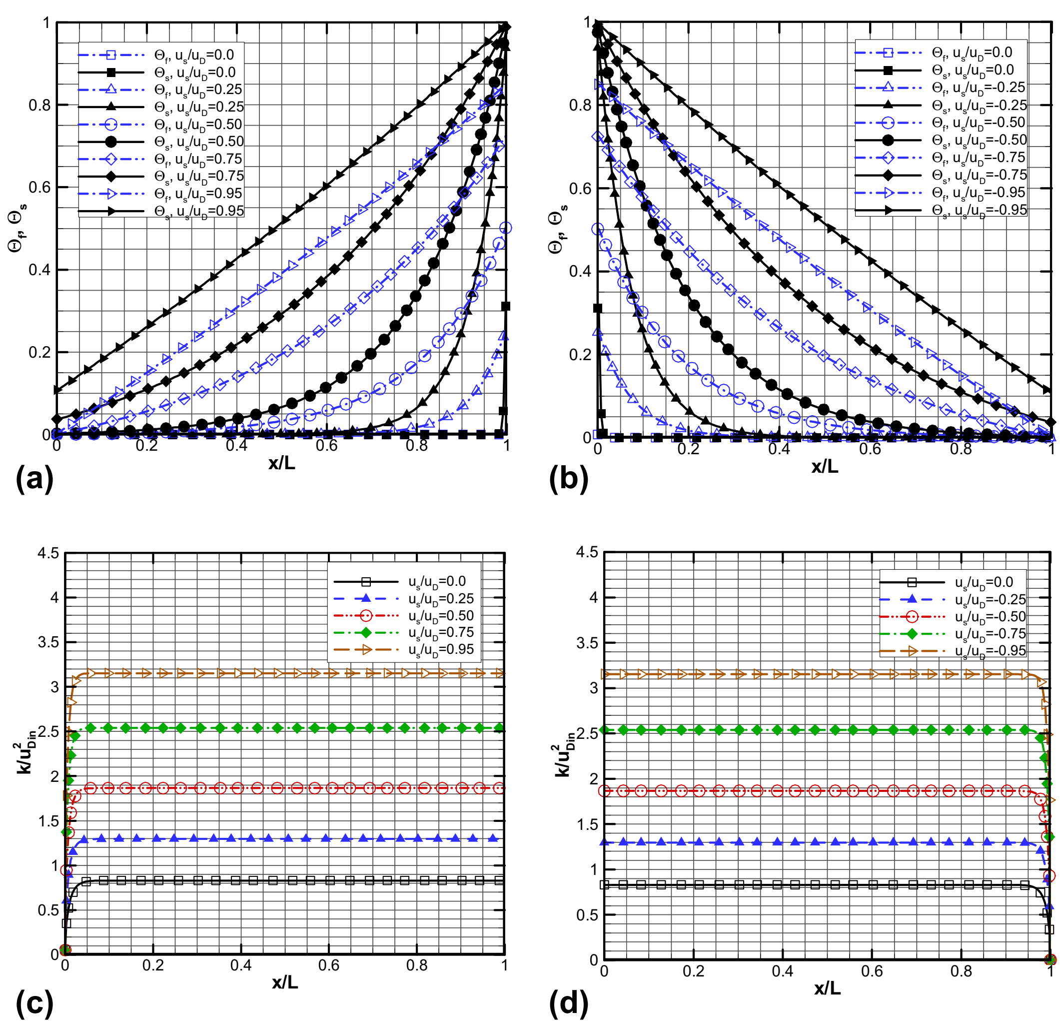


**Fig. 6.** Non-dimensional temperatures and turbulent kinetic energy for Low Reynolds number turbulence model as a function of $u_S/u_D$, with $k_s/k_f = 25$, $\phi = 0.6$, $Da = 1.665 \times 10^{-4}$, $(\rho c_p)_s/(\rho c_p)_f = 1$, $Re = 9.687 \times 10^4$: (*a*), (*c*) Flow moving west to east, (*b*), (*d*). Flow moving east to west.

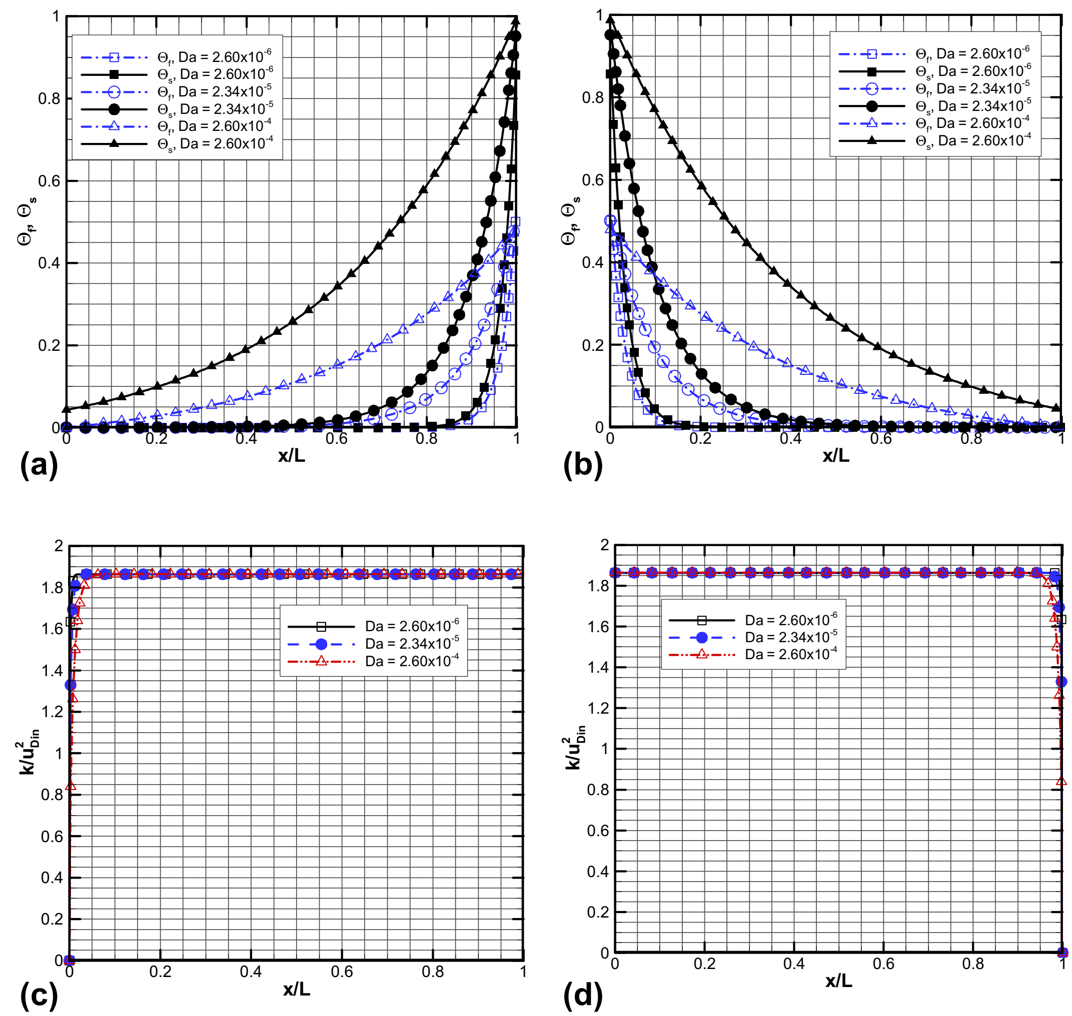


**Fig. 7.** Non-dimensional temperatures and turbulent kinetic energy for High Reynolds number turbulence model as a function of *Da*, with $u_S/\bar{u}_D = -0.5$, $(\rho c_p)_s/(\rho c_p)_f = 1$, $k_s/k_f = 25$, $\phi = 0.6$, $Re = 1.292 \times 10^6$: (*a*), (*c*) Flow moving west to east, (*b*), (*d*). Flow moving east to west.

where the subscripts *s*, *f* stands for the solid and fluid phases, respectively, and "max" and "min" refers to both temperature maximum and minimum of either phase. Also, it is interesting to mention that correctness of the energy balance of both phases was checked for every run to be presented, or say, heat leaving one phase was properly absorbed by the other.

In the following figures, results for the distribution of temperature and turbulent kinetic energy along the channel mid-height in a moving bed, for both High and Low Reynolds turbulence models, are presented. The fluid and solid phases are given different temperatures at the inlet. Data for all runs for moving bed cases are detailed in Tables 2 and 3.

Before showing the results, a note on the character of the numerical solution here adopted, namely an elliptic scheme, is here justified. Although the geometry and boundary conditions in Fig. 1 might at a first glance indicate a one-dimensional problem, which would be governed by a set of ODEs, it is important to note that surfaces at the north and south boundaries in Fig. 1*b*,*c* are solid walls, over which boundary conditions given by Eqs. (20) and (21) apply. As such, two-dimensional boundary layers will grow along the walls distorting both temperature fields requiring two-dimensional elliptical solvers, which demand 2D control volumes such as the one depicted in Fig. 2. In fact, in an accompanying paper simulation of a moving bed in cross-flow was presented [21], which required a full two-dimensional model as the one here adopted. As mentioned earlier, all results below are presented along the *x*-direction and are plotted at the channel mid-height $y/H = 0.5$.

### *2.1. Effect of Reynolds number, $Re_D$*

Figs. 3 and 4 show values for the longitudinal non-dimensional temperature profiles and for non-dimensional turbulent kinetic energy $\langle k\rangle^v/|\bar{\mathbf{u}}_D|^2$, Fig. 3c,d and Fig. 4c,d along the channel mid-height for a moving bed as a function of $Re_D$, using the both High and Low Reynolds models.

Both High and Low Reynolds numbers were calculated based on relative velocity $\bar{\mathbf{u}}_{rel}$ for a fixed slip ratio $u_S/\bar{u}_D = 0.5$ and porosity $\phi = 0.6$. As such, for increasing $Re_D$ while keeping $u_S/\bar{u}_D$ constant, both the fluid and the solid phases had to increase according to the relationship for counterflow turbulent,

$$Re_D = \frac{\rho \bar{u}_{rel} D}{\mu} = \frac{\rho \bar{u}_D D}{\mu}\left(1 - \frac{u_S}{\bar{u}_D}\right) = Re\left(1 - \frac{u_S}{\bar{u}_D}\right) \tag{35}$$

in this case, the fluid velocity $\bar{u}_D$, that is given by $\bar{u}_D = \phi < \bar{u}>^i$, increases, so there is an increase in the intrinsic fluid velocity $< \bar{u}>^i$, reflecting a greater conversion of mechanical kinetic energy into turbulence.

Fig. 3*a* and Fig. 4*a* indicate that the cold fluid is heated up as it permeates the hot porous structure, which moves in the opposite direction of the fluid. It is observed that the higher the relative Reynolds number, resulting from increasing the opposing mass flow

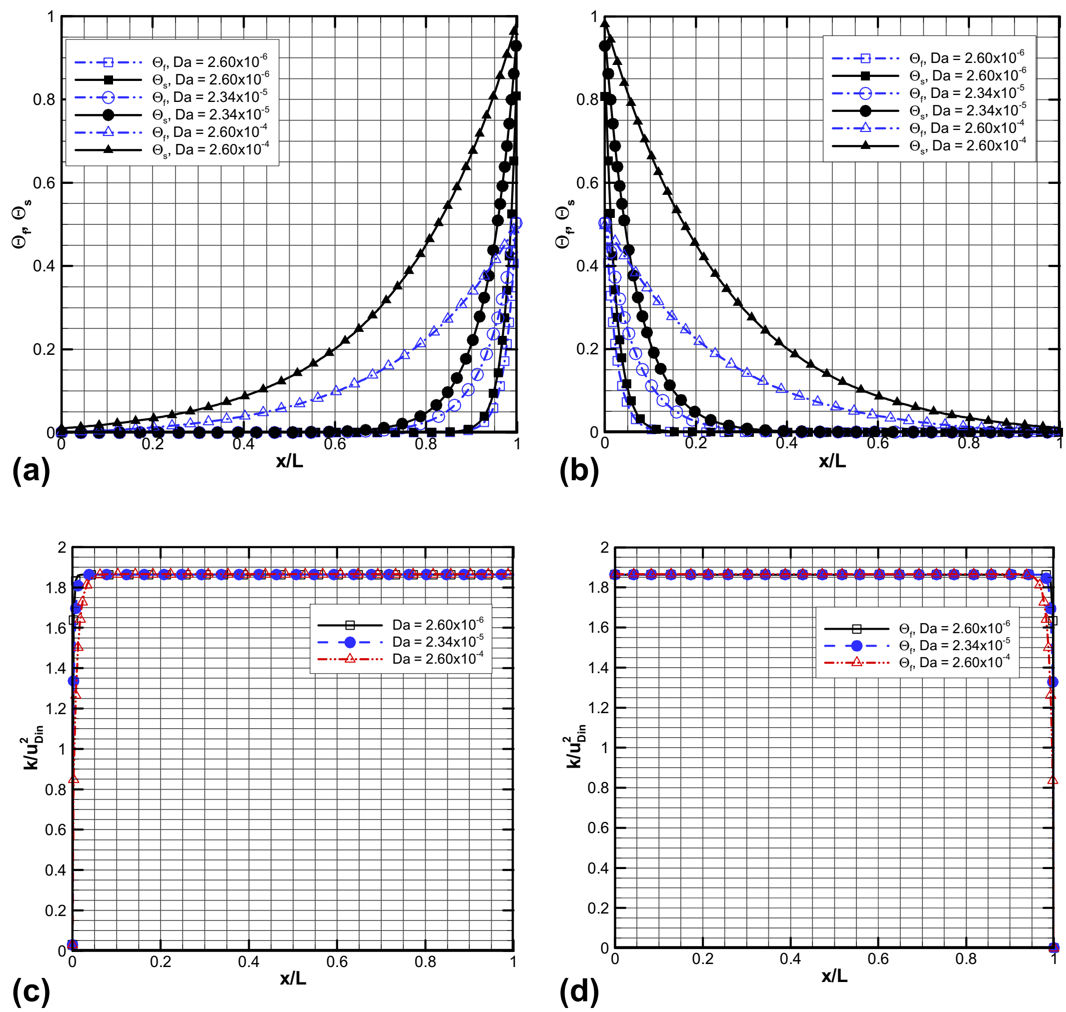


**Fig. 8.** Non-dimensional temperatures and turbulent kinetic energy for Low Reynolds number turbulence model as a function of $Da$, with $u_S/\bar{u}_D = -0.5$, $(\rho c_p)_s/(\rho c_p)_f = 1$, $k_s/k_f = 25$, $\phi = 0.6$, $Re = 1.292 \times 10^5$: (*a*), (*c*) Flow moving west to east, (*b*), (*d*). Flow moving east to west.

rates of both the fluid and the solid, with consequent increase on the relative velocity between the phases, more energy is convected into the system increasing the temperature difference between the phases along the channel. Although an increase in $Re_D$ reflects in an increase in $h_i$, Eq. (19), resulting in a stronger interstitial heat exchange, the imposed elevation of both mass flow rates in order to keep $u_S/\bar{u}_D = -0.5$ will result in larger temperature differences for the same length of the reactor. The corresponding effect is seen in Fig. 3*b* and Fig. 4*b* when both flows have their directions reversed. This behavior is the same for High and Low Reynolds models.

Fig. 3*c*,*d* and Fig. 4*c*,*d* show that when the relative velocity $\bar{\mathbf{u}}_{rel}$ increases, the amount of fluid disturbance past the solid obstacles increases, implying then in a rise of the final level of $\langle k\rangle^i$, according to $G^i = c_k\rho\phi\langle k\rangle^i|\bar{\mathbf{u}}_D|/\sqrt{K}$ for High and Low Reynolds turbulence models regardless the sense of the flow.

### 2.2. Effect of slip ratio, $\mathbf{u}_s/\bar{\mathbf{u}}_D$

Figs. 5 and 6 show values for the longitudinal non-dimensional temperature profiles $\theta_f$, $\theta_s$ and for non-dimensional turbulent kinetic energy $\langle k\rangle^v/|\bar{\mathbf{u}}_D|^2$ along the channel mid-height for a moving bed, as a function of $\mathbf{u}_s/\bar{\mathbf{u}}_D$. It is observed in Fig. 5*a* and Fig. 6*a* that the fluid speed was kept constant in one direction ($Re = 1.292 \times 10^6$ for High Reynolds and $Re = 9.687 \times 10^4$ for Low Reynolds) and the solid speed, in the opposite direction, was varied leading to the increase of absolute values of $u_S/\bar{u}_D$. It is noted that for higher absolute values of $u_S/\bar{u}_D$, or say, higher relative velocities $\bar{u}_{rel} = \bar{u}_D - u_S$, heating of the fluid is more efficient, raising its temperature at the fluid exit. The Fig. 5*a* and Fig. 6*a* indicate that increasing $u_S/\bar{u}_D$, more thermal energy is brought into the system by the solid phase, leading to an increase in the solid temperature at a certain axial position $x/L$. Due to a greater $Re_D$, which is based on $\bar{u}_{rel}$, better interstitial heat transfer is obtained, raising the fluid temperature at the same axial location. In all cases, it is observed that the outlet temperature of the fluid is greater than the outlet temperature of the solid. The corresponding effect is seen in Fig. 5*b* and Fig. 6*b* when both flows have their directions reversed. This behavior is the same for High and Low Reynolds models.

Fig. 5*c*,*d* and Fig. 6*c*,*d* indicate the increasing of turbulence kinetic energy $\langle k\rangle^v/|\bar{\mathbf{u}}_D|^2$ as the absolute values of $u_S/\bar{u}_D$ rises. As the relative velocity $\bar{\mathbf{u}}_{rel}$ increases, the amount of disturbance past the solid obstacles is increased, implying then in a rise of the final level of $\langle k\rangle^i$ for High and Low Reynolds models.

### 2.3. Effect of Darcy number, Da

Figs. 7 and 8 present the effect of particle diameter $D$ on the axial temperature profiles and non-dimensional turbulent kinetic energy $\langle k\rangle^v/|\bar{\mathbf{u}}_D|^2$ along the channel mid-height. For a give particle diameter, permeability is given according to the Ergun (1952) [20] equation:

$$K = \frac{D^2\phi^2}{144(1-\phi)^2} \tag{36}$$

leading to a Darcy number $Da = K/H^2$ where $H$ is the height of channel. The Reynolds number and the porosity are kept constant for all curves. It is observed in Fig. 7*a*) and Fig. 8*a*) that a reduction in $K$ means an increase in flow resistance. It is observed in Fig. 7*a*) and Fig. 8*a*) that for a small permeability, or small $Da = K/H^2$ as a result of a decrease of particle diameter while keeping the porosity constant, a larger interfacial heat transfer area promotes energy transfer along the channel, resulting then in a more efficient heat exchange between phases. This can be observed that the outlet temperature of the fluid is greater than the outlet temperature of the solid. The corresponding effect is seen in Fig. 7*b*) and Fig. 8*b*) when both flows have their directions reversed. This behavior is the same for High and Low Reynolds models.

The permeability of the medium exerts an effect on the level of turbulent kinetic energy along the channel, since it determines the facility that the fluid has to flow. Fig. 7*c*,*d*) and Fig. 8*c*,*d*) show the non-dimensional turbulent kinetic energy $\langle k\rangle^v/|\bar{\mathbf{u}}_D|^2$. It is observed that the higher the permeability, keeping fixed the relative velocity and the porosity, there is a decrease of the final level of $\langle k\rangle^i$, for High and Low Reynolds models. It is observed also that the decreasing of $\langle k\rangle^i$ happen mainly next to the entrance of the channel for High and Low Reynolds models. It does not matter the direction of flow in the counterflow configuration, the behavior is the same along the channel. It is noticed that the influence on the variation of the turbulent kinetic energy is more significant in the fluid inlet. Along the channel the final level of $\langle k\rangle^i$ is constant.

### 2.4. Effect of porosity, $\phi$

Figs. 9 and 10 show values for the longitudinal non-dimensional temperature profiles and for non-dimensional turbulent kinetic energy $\langle k\rangle^v/|\bar{\mathbf{u}}_D|^2$ along the channel mid-height for a moving bed, as a function of porosity $\phi$. The Reynolds number $Re_D$, the velocity ratio between the solid and fluid phases $u_S/\bar{u}_D = -0.5$ and the ratio of thermal capacity $(\rho c_p)_s/(\rho c_p)_f = 1$ are kept constant for all curves. The Fig. 9*a*) and Fig. 10*a*) indicate that, for low porosities, a better heat exchange is obtained between phases. For a fixed Reynolds number, a decrease in porosity corresponds to an increase on the interfacial heat transfer coefficient $h_i$, Eq. (19). Also, for a fixed Reynolds number based on $u_D = \phi < u >^i$, a decrease in porosity corresponds to an increase in the intrinsic fluid velocity $\langle u\rangle^i$, reflecting a greater conversion of mechanical kinetic energy into turbulence, which further rises the cooling effect by raising the interfacial heat transfer coefficient $h_i$ between phases. Consequently, the product $h_ia_i$ will increase as porosity $\phi$ decreases, enhancing the ability of the solid phase to heat up the colder fluid. Moreover, the lower the porosity, *i.e.*, the greater the amount of solid material per total

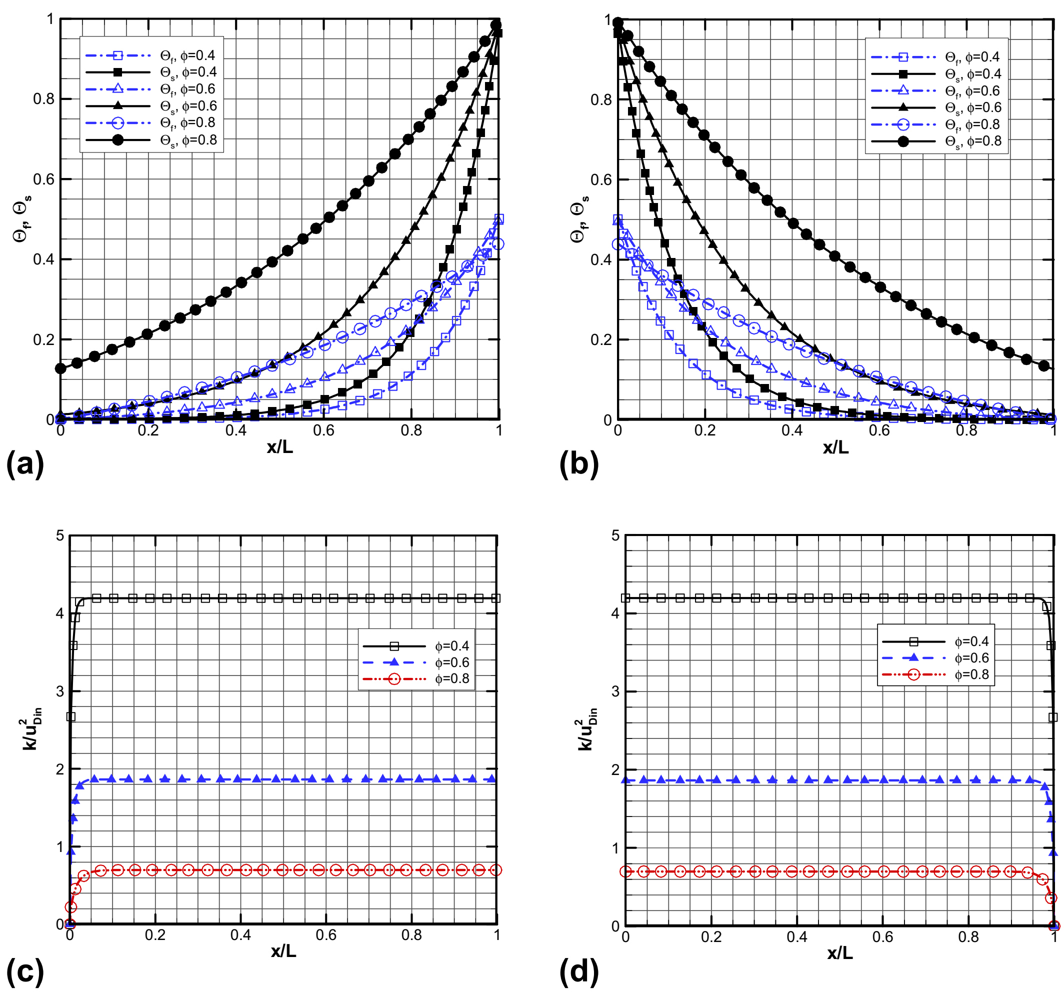


**Fig. 9.** Non-dimensional temperatures and turbulent kinetic energy for High Reynolds number turbulence model as a function of $\phi$, with $u_S/u_D = -0.5$, $k_s/k_f = 25$, $Re_D = 5 \times 10^4$ and $Re = 6.458 \times 10^5$: (*a*), (*c*) Flow moving west to east, (*b*), (*d*). Flow moving east to west.

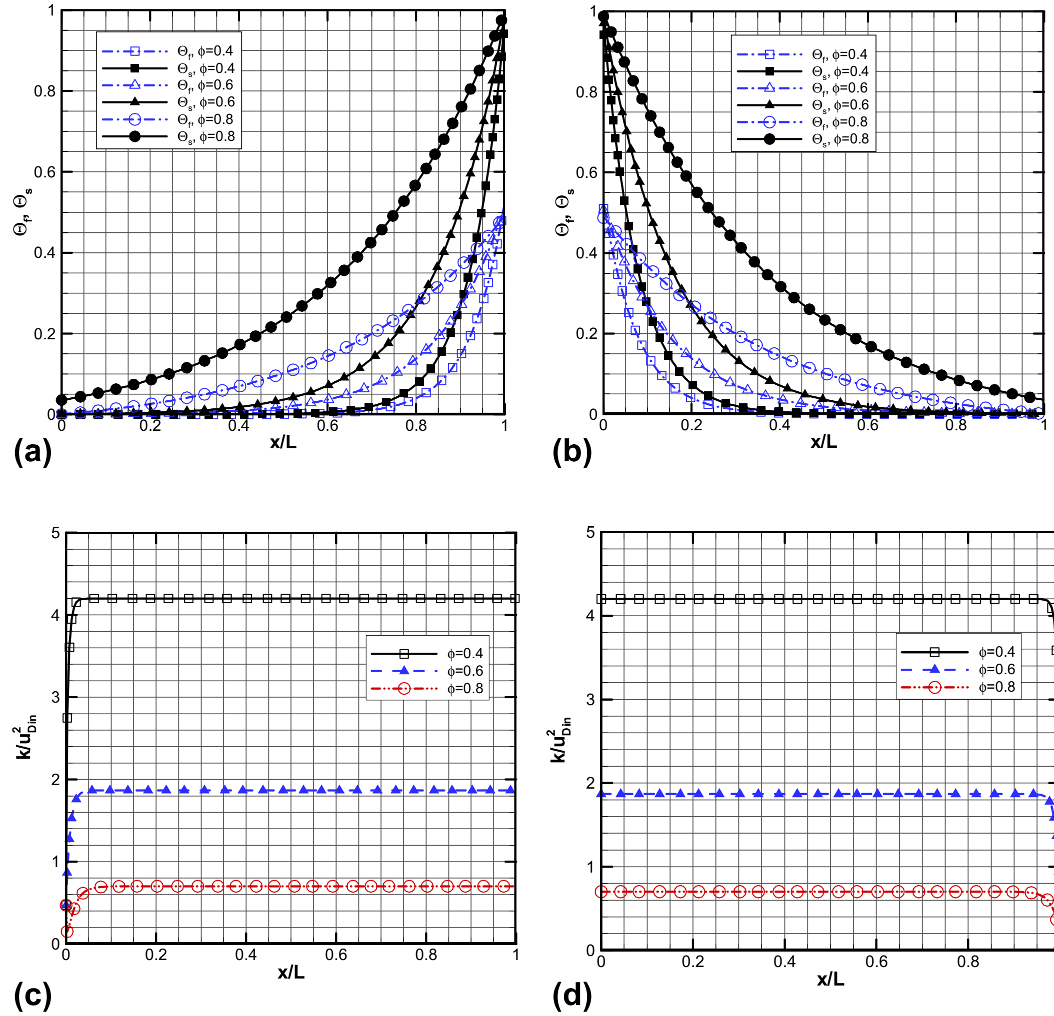


**Fig. 10.** Non-dimensional temperatures and turbulent kinetic energy for Low Reynolds number turbulence model as a function of $\phi$, with $u_S/u_D = -0.5$, $k_s/k_f = 25$, $Re_D = 2.5 \times 10^3$ and $Re = 3.229 \times 10^4$: (*a*), (*c*) Flow moving west to east, (*b*), (*d*). Flow moving east to west.

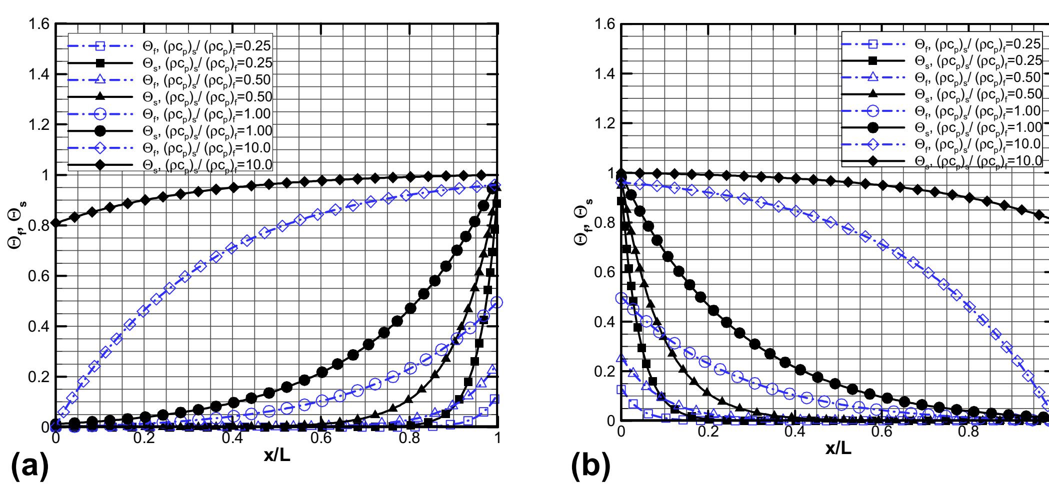


**Fig. 11.** Non-dimensional temperatures for High Reynolds number turbulence model as a function of $(\rho c_p)_s/(\rho c_p)_f$, with $u_S/\bar{u}_D = -0.5$, $k_s/k_f = 25$, $\phi = 0.6$, $Re_D = 5 \times 10^4$, $Re = 6.458 \times 10^5$: (*a*) Flow moving west to east, (*b*). Flow moving east to west.

volume, the fluid temperature will be closer to that of the solid temperature along the channel, which is caused by a greater exchange of heat between phases. This can be observed that the outlet fluid temperature is greater than the solid temperature at exit for all values of porosity used. The corresponding effect is seen in Fig. 9*b*) and Fig. 10*b*) when both flows have their directions

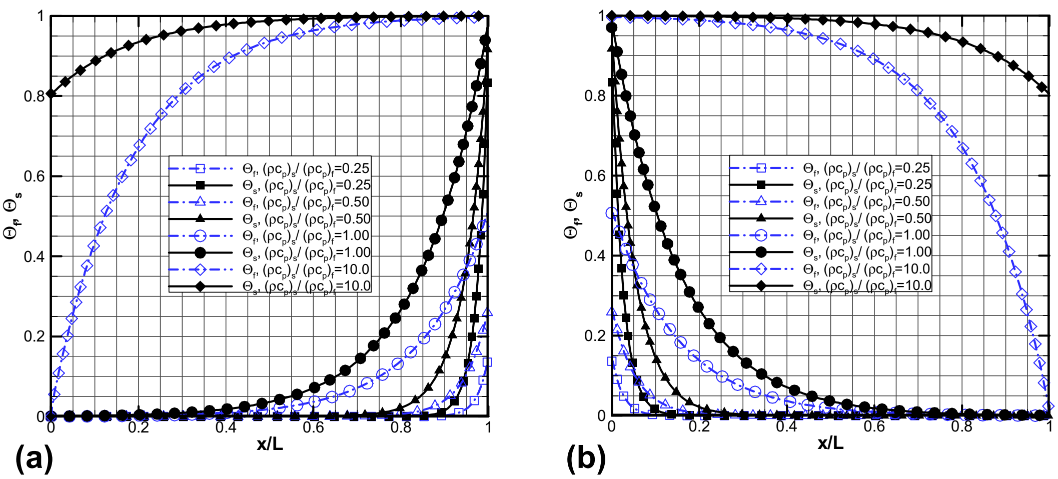


**Fig. 12.** Non-dimensional temperatures for Low Reynolds number turbulence model as a function of $(\rho c_p)_s/(\rho c_p)_f$, with $u_s/\bar{u}_D = -0.5$, $k_s/k_f = 25$, $\phi = 0.6$, $Re_D = 2.5 \times 10^3$, $Re = 3.229 \times 10^4$: (*a*) Flow moving west to east, (*b*) Flow moving east to west.

reversed. This behavior is the same for High and Low Reynolds models.

Fig. 9*c,d*) and Fig. 10*c,d*) show the non-dimensional turbulent kinetic energy $\langle k\rangle^v/|\bar{\mathbf{u}}_D|^2$. It is observed that the higher the porosity, keeping fixed the relative velocity and the permeability, there is a decrease of the final level of $\langle k\rangle^i$ for High and Low Reynolds models. It does not matter the direction of flow in the counterflow configuration, the behavior is the same along the channel.

### 2.5. Effect of thermal capacity ratio $(\rho c_p)_s/(\rho c_p)_f$

Figs. 11 and 12 show values for the longitudinal non-dimensional temperature profiles along the channel mid-height for a moving bed, as a function of thermal capacity ratio (ρcp)s/(ρcp)f. The density and specific heat of the fluid are kept constant given by ρf = 0.4345 kg/m3 and cpf = 1986.8 J/kgK, respectively. It is observed in Fig. 11a) and Fig. 12b) that when the heat capacity of the solid is greater than the fluid, the solid temperature presents less variation in temperature across the reactor. When the thermal capacity of the solid (ρcp)s is high, more energy exchange is needed to vary the temperature of the solid by a certain amount. Also, for all cases, the outlet fluid temperature is greater than the value of the solid temperature at the exit. For the highest ratio analyzed, (ρcp)s/(ρcp)f = 10.0, the solid temperature undergoes the least variation, as expected. The corresponding effect is seen in Fig. 11b) and Fig. 12b) when both flows have their directions reversed. This behavior is the same for High and Low Reynolds models.

How the variation of the thermal capacity ratio does not affect the final level of the kinetic energy, this effect is not shown here.

### 2.6. Effect of thermal conductivity ratio $k_s/k_f$

Figs. 13 and 14 show values for the longitudinal non-dimensional temperature profiles along the channel mid-height for a moving bed, as a function of thermal conductivity ratio $k_s/k_f$. For a fixed solid substrate, $u_s/u_D = 0$ (Fig. 13*a* and Fig. 14*a*), one note that the higher the ratio $k_s/k_f$, the stronger is the axial conduction through the solid, raising its temperature and, consequently, heating up the fluid at the outlet.

With the slow movement of the solid bed, $u_s/u_D = -0.1$, Fig. 13*c,d* and Fig. 14*c,d* show that the solid temperature is raised not only by axial conduction along the bed, but also due to increase of the fluid temperature due to a better exchange of heat between phases, an effect caused by increase of the interfacial heat transfer coefficient $h_i$, which, in turn, is a result of increasing the relative velocity and, consequently, $Re_D$. As a result, values of both the fluid and the solid temperatures along the channel increase with $k_s/k_f$. Compared to the previous case for $u_s/u_D = 0$, the effect of $k_s/k_f$ now seems to be of a lesser importance since inter-phase heat transport starts to play a role in temperature distributions as the solid velocity increases. Such conclusion becomes more evident for $u_s/u_D = -0.4$ (Fig. 13*e,f* and Fig. 14*e,f*), when the ratio of thermal conductivity causes little influence on the temperature distribution within each phase along the channel. For high solid mass flow rates, with absolute values of $u_s/u_D$ approaching to 1, there is a better heat exchange between the phases along the channel, regardless of the value of the thermal conductivity of the solid. This behavior is the same for High and Low Reynolds models.

The variation of $k_s/k_f$ does not affect the turbulent kinetic energy for this reason they are not presented here. In the case of the fluid and solid temperatures, it is observed, according to the results obtained here, that the movement of the solid material contrary to the direction of the fluid, with higher $Re_D$ or slip ratio $u_s/u_D$, enhances heat transfer between phases.

## 3. Conclusions

This paper investigated the behavior of a two-energy equation model to simulate the influence of physical properties on heat transfer between solid and fluid phases in a turbulent moving bed counterflow using the High and Low Reynolds models, in which the working fluid flows in opposite direction with respect to the permeable medium. Numerical solutions for turbulent flow in a moving porous bed were obtained for different Reynolds number $Re_D$, slip ratio $\mathbf{u}_s/\bar{\mathbf{u}}_D$, Darcy number $Da$, porosity $\phi$, ratio of thermal capacity $(\rho c_p)_s/(\rho c_p)_f$ and of ratio of thermal conductivity $k_s/k_f$, ranging the slip ratio $\mathbf{u}_s/\bar{\mathbf{u}}_D$.

Governing equations were discretized and numerically solved. It is observed, according with the results obtained, that the heat exchange between phases is more efficient when compared with parallel flow cases. Movement of the solid material contrary to the direction of the fluid, with higher $Re_D$ or slip ratio $u_s/u_D$, enhances heat transfer between phases. Same effect was observed for smaller $Da$, smaller $\phi$, and higher $(\rho c_p)_s/(\rho c_p)_f$ and $k_s/k_f$. This results are similar with those showed in [10] for laminar counterflow.

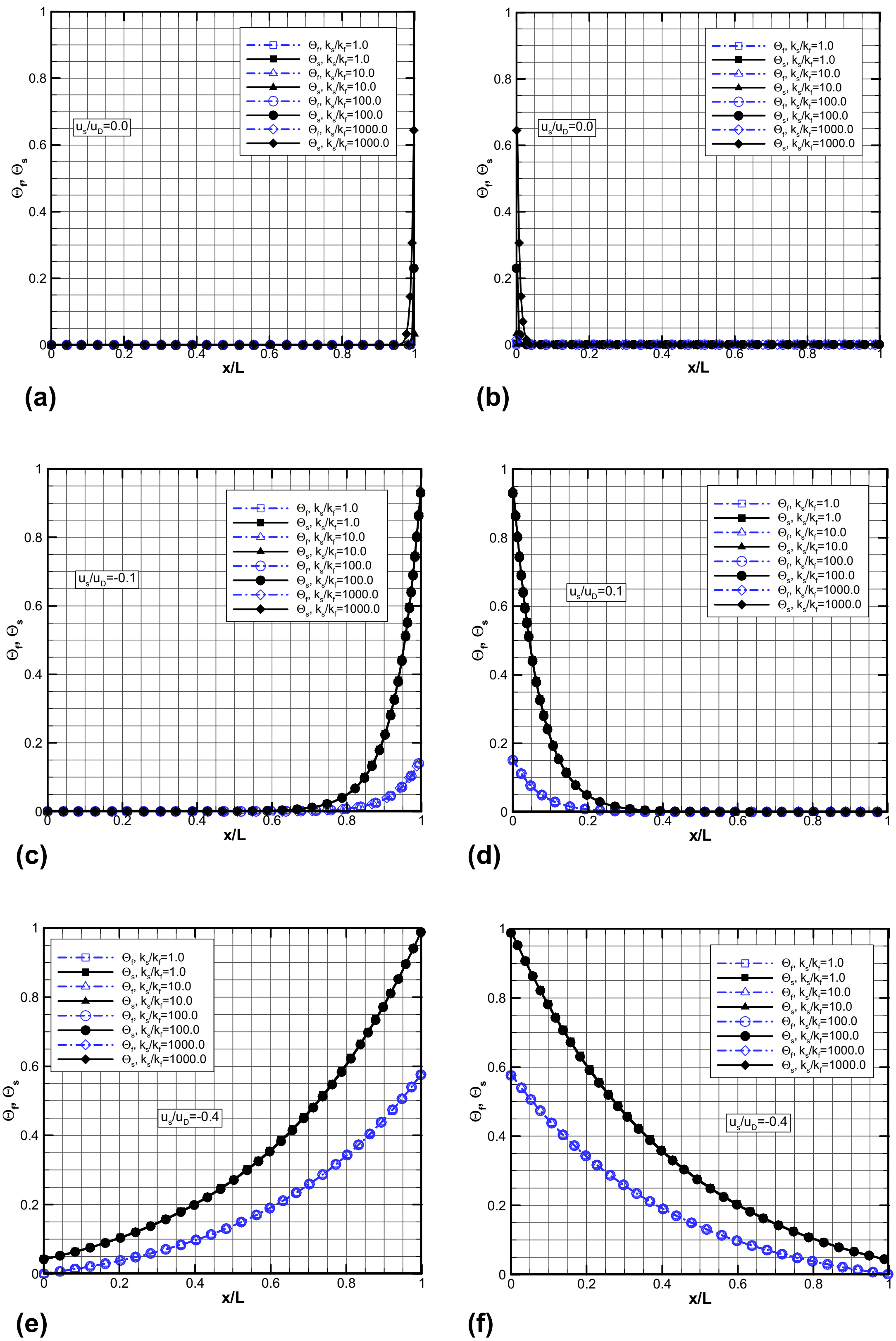


**Fig. 13.** Non-dimensional temperatures for High Reynolds number turbulence model as a function of $k_s/k_f$, with $\phi = 0.6$, $Da = 1.665 \times 10^{-4}$, $(\rho c_p)_s/(\rho c_p)_f = 1$, $Re_D = 5 \times 10^4$: (*a*), (*c*), (*e*) Flow moving west to east, (*b*), (*d*), (*f*). Flow moving east to west.

For high values of $Re_D$ and high absolute values of $\mathbf{u}_s/\bar{\mathbf{u}}_D$ the higher the final level of $\langle k \rangle^i$, in other hand, for high values of $Da$ and $\phi$ the smaller the final level of $\langle k \rangle^i$. The similar behavior was observed for High and Low Reynolds model.

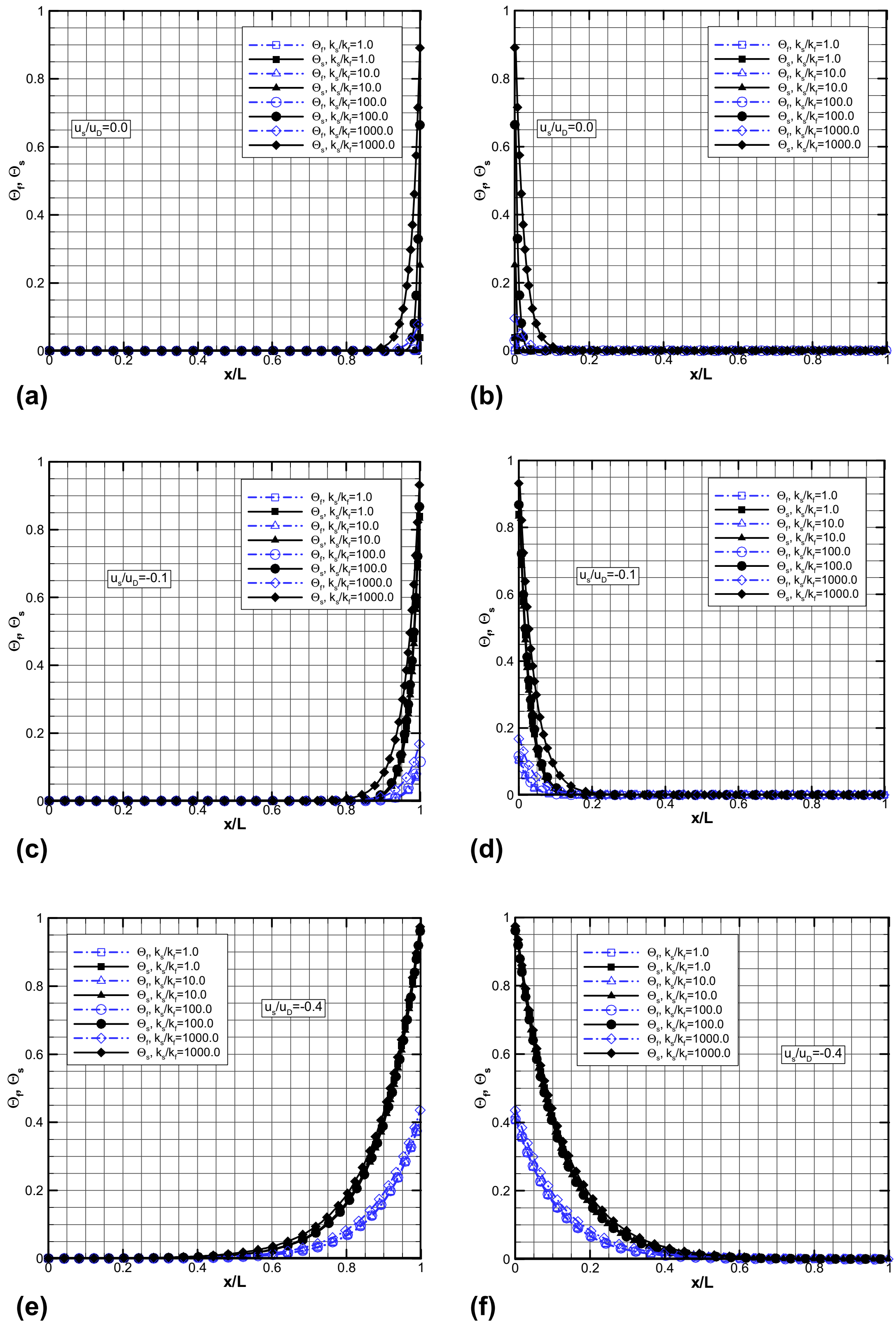


**Fig. 14.** Non-dimensional temperatures for Low Reynolds number turbulence model as a function of $k_s/k_f$, with $\phi = 0.6$, $Da = 1.665 \times 10^{-4}$, $(\rho c_p)_s/(\rho c_p)_f = 1$, $Re_D = 2.5 \times 10^3$: (*a*), (*c*), (*e*) Flow moving west to east, (*b*), (*d*), (*f*). Flow moving east to west.

## Acknowledgments

The authors are thankful to CNPq and FAPESP, Brazil, for their invaluable financial support during the course of this research.

## References

[1] Y. Yang, M. Hwang, Numerical simulation of turbulent fluid flow and heat transfer characteristics in heat exchangers fitted with porous media, Int. J. Heat Mass Transfer 52 (2009) 2956–2965.
[2] H. Littman, M.H. Morgan III, S.D. Jovanovic, J.D. Paccione, Z.B. Grbavcic, D.V. Vukovic, Effect of particle diameter, particle density and loading ratio effective drag coefficient in steady turbulent gas-solids transport, Powder Technol. 84 (1995) 49–56.
[3] Z. Mansoori, M. Saffar-Avval, H. Basirat-Tabrizi, G. Ahmadi, S. Lain, Thermo-mechanical modeling of turbulent heat transfer in gas-solid flows including particle collisions, Int. J. Heat Fluid Flow 23 (2002) 792–806.
[4] Y. Zhang, J.M. Reese, Particle-gas turbulence interactions in a kinetic theory approach to granular flows, Int. J. Multiphase Flow 27 (2001) 1945–1964.
[5] A.V. Kuznetsov, M. Xiong, Development of an engineering approach to computations of turbulent flows in composite porous/fluid domains, Int. J. Therm. Sci. 42 (10) (2003) 913–919.
[6] A.V. Kuznetsov, L. Cheng, M. Xiong, Effects of thermal dispersion and turbulence in forced convection in composite parallel-plate channel: investigation of constant wall heat flux and constant wall temperature cases, Numer. Heat Transfer Part A 42 (4) (2002) 365–383.
[7] M.J.S. de Lemos, Turbulence in Porous Media: Modeling and Applications, 2nd. Ed., Elsevier, Oxford, 2012.
[8] M.B. Saito, M.J.S. de Lemos, A macroscopic two-energy equation model for turbulent flow and heat transfer in highly porous media, Int. J. Heat Mass Transfer 53 (2010) 2424–2433.
[9] A.C. Pivem, M.J.S. de Lemos, Laminar heat transfer in a moving porous Bed reactor simulated with a macroscopic two-energy equation model, Int. J. Heat Mass Transfer 55 (7–8) (2012) 1922–1930.
[10] A.C. Pivem, M.J.S. de Lemos, Temperature distribution in a counterflow moving bed under a thermal nonequilibrium condition, Numer. Heat Transfer 61 (2012) 1–17.
[11] W.G. Gray, P.C.Y. Lee, On the theorems for local volume averaging of multiphase system, Int. J. Multiphase Flow 3 (1977) 333–340;
S. Whitaker, Advances in theory of fluid motion in porous media, Ind. Eng. Chem. 61 (1969) 14–28.
[12] S. Whitaker, Diffusion and dispersion in porous media, J. Am. Inst. Chem. Eng. 13 (3) (1967) 420–427.
[13] B.E. Launder, D.B. Sapalding, The numerical computation of turbulent flows, Comput. Meth. Appl. Mech. Eng. 3 (1974) 269–289.
[14] K. Abe, Y. Nagano, T. Kondoh, An improve $k-\varepsilon$ model for prediction of turbulent flows with separation and reattachment, Trans. JSME 58 (1992) 3003–3010.
[15] M.B. Saito, M.J.S. de Lemos, A correlation for interfacial heat transfer coefficient for turbulent flow over an array of square rods, J. Heat Transfer 128 (2006) 444–452.
[16] F. Kuwahara, M. Shirota, A. Nakayama, A numerical study of interfacial convective heat transfer coefficient in two-energy equation model for convection in porous media, Int. J. Heat Mass Transfer 44 (2001) 1153–1159.
[17] M.J.S. de Lemos, M.B. Saito, Interfacial Heat Transport in Highly Permeable Media: A Finite Volume Approach, in: A. Ochsner, G.E. Murch, M.J.S. de Lemos (Eds.), Cellular and Porous Materials: Thermal Properties Simulation and Prediction, WILEY-VCH Verlag, Weinheim, 2008. Chapter 1.
[18] S.V. Patankar, Numerical Heat Transfer and Fluid Flow, Hemisphere, Washington, DC, 1980.
[19] H. Guoxin, X. Wei, L. Yaqin, Heat transfer and gas flow through feed stream within horizontal pipe, Transp. Porous Media 52 (2003) 371–387.
[20] S. Ergun, Fluid flow through packed columns, Chem. Eng. Process 48 (1952) 89–94.
[21] A.C. Pivem, M.J.S. de Lemos, Numerical simulation of a crossflow moving porous bed Using a thermal non-equilibrium model, Int. J. Heat Mass Transfer 67 (2013) 311–325.